Stability of the time-dependent configuration-interaction-singles method in the attosecond and strong-field regimes: A study of basis sets and absorption methods

Stefan Pabst,[1,2,*] Arina Sytcheva,[2] Otfried Geffert,[2] and Robin Santra[2,3,†]

[1]*ITAMP, Harvard-Smithsonian Center for Astrophysics, 60 Garden Street, Cambridge, Massachusetts 02138, USA*
[2]*Center for Free-Electron Laser Science, DESY, Notkestrasse 85, 22607 Hamburg, Germany*
[3]*Department of Physics, University of Hamburg, Jungiusstrasse 9, 20355 Hamburg, Germany*

We investigate the behavior of several spatial grid methods and complex absorbers for strong-field and attosecond scenarios when using the time-dependent configuration-interaction singles method to solve the multi-electron time-dependent Schrödinger equation for atoms. We compare the pseudospectral grid, finite-element, and finite-element-discrete-variable-representation (DVR) methods with each other and discuss their advantages and disadvantages. Additionally, we study the performances of complex absorbing potential (CAP) and smooth exterior complex scaling (SES) to absorb the outgoing electron. We find that SES performs generally better than CAP for calculating high-harmonic generation spectra and XUV photoelectron spectra. In both of these cases, the DVR and even more the FEM grid representations show more reliable results—especially when using SES. Both absorbers show drawbacks when calculating photoelectron spectra in the strong-field regime.

I. INTRODUCTION

Attosecond and strong-field physics is a fast moving and ever changing field. Over the years, many new techniques have been developed to probe electronic motion in atoms, molecules, and solids on their fundamental timescale [1–3]. One of the most prominent processes is high-harmonic generation (HHG) [4–7], where low-frequency optical or infrared light is converted into high-frequency EUV or soft-x-ray radiation [8]. HHG is the most dominating method for producing attosecond pulses [9]. HHG has also been used to probe orbital structure [10–13] and electronic [14,15] and nuclear motion [16–19]. Furthermore, multi-orbital [13,20,21] and electronic correlation effects [11,22,23] can play an important role and in turn can be studied with HHG and other strong-field processes.

To probe ultrafast motion, the dynamics is usually encoded in the emitted light spectrum (e.g., HHG and transient absorption [24,25]) or in the photoelectron spectrum (e.g., streaking [26] and the reconstruction of attosecond beating by interference of two-photon transitions, or RABITT [27]). They are ideal probing tools to study electronic correlation dynamics which may or may not be modified by an external laser pulse. Both aspects have been demonstrated in helium by measuring photons via transient absorption spectroscopy [28] and photoelectrons via RABITT [29].

Understanding field-driven and field-free many-body dynamics on a fundamental level requires time-dependent many-body methods (e.g., time-dependent R matrix [30,31], TD-CIS [32], and TD-SCF methods [33–35]). Describing many-body processes on top of nonlinear field-driven dynamics is numerically challenging and requires large configuration spaces. Choosing an advantageous grid can significantly improve numerical convergence and reduce numerical demand. For atoms, it is natural to exploit spherical symmetry. The angular part can be treated analytically and only the radial degree of freedom has to be solved numerically. Nevertheless, calculating the electronic dynamics in strong-field physics remains challenging because tightly bound states as well as highly delocalized continuum states need to be described for an accurate description.

The introduction of an absorbing boundary [36–39] in the form of complex absorbing potentials (CAP) [40], window functions [41], or complex scaling (CS) [42,43] is natural as one tries to keep the radial grid as small as possible. Absorbers are generally not perfect (i.e., reflection free) and introduce unphysical motion. Consequently, having a well-behaved absorber is desirable to ensure meaningful results. In particular, calculated photoelectron spectra are quite sensitive to the absorber [44].

In previous studies [42,45,46], hard-exterior complex scaling has been commonly used. Hard scaling means that the complex contour starts abruptly at a given radius. Using a specific set of B-splines allows one to deal with the kink. Smooth-exterior complex scaling (SES) [37,47] follows the idea to rotate smoothly the radial coordinate into the complex plane allowing one to use a broader variety of grid representations.

In this study, we investigate the performances of three different radial grid representations as they are used in TDCIS: pseudospectral grid (PSG), finite-element (FEM), and finite-element-discrete-variable-representation (DVR) methods. The basis functions of PSG and DVR are pseudolocal functions such that local operators, $V(\hat{r})$ turn into diagonal matrices with the diagonal entries $V(r_i)$, where r_i are the radial grid points. Numerically, a diagonal representation is very desirable but this approximation can lead to instabilities for rapidly varying potentials. Furthermore, we compare the CAP with the SES absorber for strong-field ionization and photoionization processes and study their dependence on the radial grid representation.

In Sec. II, we briefly discuss the basics of TDCIS (Sec. II A), present all three grid methods (Sec. II B) and both absorber methods (Sec. II C). All aspects are implemented in the

*stefan.pabst@cfa.harvard.edu
†robin.santra@cfel.de

XCID program [48]. Before presenting the results for HHG in hydrogen in Sec. III A, we discuss the convergence behavior of several physical and numerical parameters for the length and velocity gauges in Sec. III A 1. Photoelectron spectra using the t-SURFF method [44,49] are presented in Sec. III B for one-photon (Sec. III B) and multiphoton (Sec. III C) ionization. Atomic units (a.u.) are used throughout unless otherwise indicated.

II. METHODOLOGY

A. Time-dependent configuration interaction singles

The N-electron wave function ansatz for TDCIS reads [50]

$$|\Psi(t)\rangle = \alpha_0(t)|\Phi_0\rangle + \sum_{i,a} \alpha_i^a(t)|\Phi_i^a\rangle, \tag{1}$$

where $|\Phi_0\rangle$ is the Hartree–Fock ground state, and $|\Phi_i^a\rangle = \hat{c}_a^\dagger \hat{c}_i |\Phi_0\rangle$ are one-particle–one-hole (1p-1h) excitations where an electron from orbital i is promoted to orbital a. The indices i,j are used to refer to occupied one-particle orbitals and the indices a,b are used to refer to virtual (unoccupied) orbitals. The indices p,q refer to both (occupied and virtual) orbitals.

In the case of hydrogen, $|\Phi_0\rangle$ is just the $1s$ orbital. For multi-electron atoms, we restrict ourselves to closed-shell atoms where each occupied orbital in the HF ground state, $|\Phi_0\rangle$, is doubly occupied and the full ground state is a spin-singlet state ($S = 0$). The electric field of the laser pulse does not change the spin so that it is beneficial to use spin-symmetrized 1p-1h configurations [32,40],

$$|\Phi_i^a\rangle = \frac{1}{\sqrt{2}}\big(|\Phi_{i,\uparrow}^{a,\uparrow}\rangle + |\Phi_{i,\downarrow}^{a,\downarrow}\rangle\big), \tag{2}$$

where the spin of the electron is explicitly stated. Additional symmetries can be found to reduce the computational cost [20,51]. The time-dependent Schrödinger equation reads

$$i\frac{\partial}{\partial t}|\Psi(t)\rangle = [\hat{H}_0 + \hat{H}_1 - E_{\text{HF}} - \hat{H}_{\text{LM}}(t)]|\Psi(t)\rangle, \tag{3}$$

where $\hat{H}_0 = \hat{F} + \hat{W}$ is the Fock operator $\hat{F}$ plus the complex absorber $\hat{W}$. The residual Coulomb interaction $\hat{H}_1$ captures all the effects beyond the mean-field potential, where the latter is included in $\hat{F}$. The detailed form of $\hat{H}_1$ can be found in Refs. [32,40]. For hydrogen, $\hat{H}_1 = 0$ because there is only one electron. The light-matter interaction can be written in the length (LG) or velocity (VG) form,

$$\hat{H}_{\text{LM}}(t) = \begin{cases} \vec{\mathcal{E}}(t) \cdot \hat{\mathbf{r}}, & \text{(LG)} \\ \vec{\mathcal{A}}(t) \cdot \hat{\mathbf{p}}, & \text{(VG)}, \end{cases} \tag{4}$$

where $\vec{\mathcal{E}}(t) = -\partial_t \vec{\mathcal{A}}(t)$ is the electric field and $\vec{\mathcal{A}}(t)$ is the vector potential [52]. Both forms are equivalent and, if no approximations are made, all physical observables are independent of the choice of gauge. However, the convergence behavior of these gauges is different and TDCIS, as all configuration interaction (CI) theories (except full CI), is not gauge invariant [53]. In Sec. III A 1, we study the gauge-dependent convergence in the strong-field regime for hydrogen. We restrict ourselves to linearly z polarized light in the following.

Projecting Eq. (3) onto $\langle\Phi_0|$ and $\langle\Phi_i^a|$, we obtain the equation of motion for all time-dependent coefficients:

$$i\dot{\alpha}_0(t) = \sum_{a,i} \langle\Phi_0|\hat{H}_{LM}(t)|\Phi_i^a\rangle \alpha_i^a(t), \tag{5a}$$

$$i\dot{\alpha}_i^a(t) = (\varepsilon_a - \varepsilon_i)\alpha_i^a(t) + \langle\Phi_i^a|\hat{H}_{LM}(t)|\Phi_0\rangle\alpha_0(t)$$
$$+ \sum_{b,j} \langle\Phi_i^a|\hat{H}_{LM}(t) + \hat{H}_1|\Phi_j^b\rangle\alpha_j^b(t), \tag{5b}$$

where $|\Phi_i^a\rangle := |\Phi_i^a\rangle$ and $\langle\Phi_i^a|$ are right and left eigenstates, respectively, of the non-Hermitian Fock operator $\hat{H}_0$ (see Refs. [32,37]). The non-Hermiticity comes from the complex absorber $\hat{W}$. The energies of the occupied and virtual orbitals, $\hat{H}_0|\varphi_p\rangle = \varepsilon_p|\varphi_p\rangle$, are given by ε_i and ε_a, respectively. The orbital energies ε_a are complex because of the complex absorber (see Sec. II C). The absorber is chosen to be far away from the atom such that the occupied orbitals are not affected by the absorber and their energies stay real.

Not all virtual orbitals a need to be considered to obtain converged results. We restrict ourselves to orbitals with angular momentum up to $l_{\max}$ and orbital energies where the real part is smaller than e_c. The specific choices of $l_{\max}$ and e_c and how they depend on the light-matter gauge are discussed in Sec. III A 1.

B. Radial representations

For atomic systems, the one-particle orbitals can be written as angular-momentum eigenstates,

$$\varphi_p(\mathbf{r}) = \frac{u_{n,l}(r)}{r} Y_{l,m}(\theta,\phi), \tag{6}$$

where $Y_{lm}(\theta,\phi)$ are spherical harmonics and $u_{nl}(r)$ are radial functions depending on the radial quantum number n and the angular momentum l. Since the angular part and the corresponding integrals are analytically known, only the radial degree of freedom has to be solved on a numerical grid. In terms of the underlying radial basis functions $b_i(r)$, the radial function $u_{n,l}(r)$ reads

$$u_{n,l}(r) = \sum_i u_{n,l}^i b_i(r). \tag{7}$$

In the following, we discuss three different sets of basis functions: pseudospectral grid method (PSG), finite-element method (FEM), and finite-element-based discrete-variable representation (FEM-DVR or just DVR). For the PSG method, the basis functions are the cardinal functions $g_k(r)$. The FEM basis functions are written as $\kappa_j^{(i)}(r)$ and the DVR basis functions are written as $\nu_k(r)$. The properties of the different basis functions are explained below.

For all grid methods, we enforce the boundary conditions $u_{n,l}(r = 0) = u_{n,l}(r_{\max}) = 0$. The enforcement at $r_{\max}$ introduces artificial reflections which are prevented by the absorber (see Sec. II C). Independent of the grid method, we choose a mapping

$$r(x) = \frac{r_{\max}\zeta}{2}\frac{1+x}{1-x+\zeta}, \tag{8}$$

with $x \in [-1,1]$ so that near the origin we have a denser grid for the bound states, and further out it approaches a linear distribution for describing the continuum states. The parameter ζ regulates the local density of points: the smaller is ζ, the more points are located near the origin.

For FEM and DVR, this mapping is used to define the reference points around which the FEM functions are defined. The x points are chosen to be equidistant. The number of radial basis functions is $N_b = 3N - 2$, where N is the number of x points (including $x = \pm 1$). For the PSG method, the Hamiltonian is expressed explicitly in terms of x [32]. With N points in the x domain (including $x = \pm 1$) we get $N_b = N - 2$ radial basis functions for the PSG method.

1. Pseudospectral grid

The pseudospectral grid method (PSG), which is based on the Gauss–Lobatto quadrature, has been described in detail in Refs. [54–56]. We briefly review the main aspects. A function $f(x)$ on the interval $[-1,1]$ may be expressed in terms of Legendre polynomials, $P_k(x)$:

$$f(x) \approx f_N(x) = \sum_{k=0}^{N-1} a_k P_k(x), \qquad (9)$$

which may also be written in terms of cardinal functions $g_k(x)$,

$$f_N(x) = \sum_{k=0}^{N-1} f(x_k) g_k(x), \qquad (10)$$

where we require that the approximation yields the exact value of the function $f(x_k)$ at each grid point x_k. The N grid points are given by the zeros of the first derivative of $P_{N-1}(x)$ and the endpoints $x = \pm 1$. The cardinal functions have the form [43]

$$g_k(x) = -\frac{1}{N(N-1)P_{N-1}(x_k)} \frac{(1-x^2)P'_{N-1}(x)}{x - x_k} \qquad (11)$$

and satisfy the unique property $g_k(x_l) = \delta_{kl}$. From Eq. (11), analytic expressions for the first and second derivatives can be derived [54,56]. To evaluate local potentials, $V(x) := V(r(x))$, only their values at the grid points, $V(x_k)$, need to be known. This is an approximation once the product of the local potential with the two orbitals appearing in the radial integral is a polynomial of order larger than $2N - 3$ (or is not a polynomial at all), which is generally the case because orbitals have exponential dependencies and the Coulomb potential is not a polynomial potential. Due to the boundary conditions, $u_{n,l}(0) = u_{n,l}(r_{\max}) = 0$, only $N - 2$ radial basis functions exist for N grid points.

2. Finite-element method

Finite-element methods (FEMs) are based on functions localized around a set of reference points r_i. The distribution of these reference points can be chosen arbitrarily. However, we use the mapping of Eq. (8) to define the reference points r_i with $i = 1, \ldots, N$. In this way, we have a more direct comparison between the grid methods. We use the FE functions from Refs. [57,58]. On the interval $[0,1]$ we construct six unique, linearly independent fifth-order Hermite interpolating
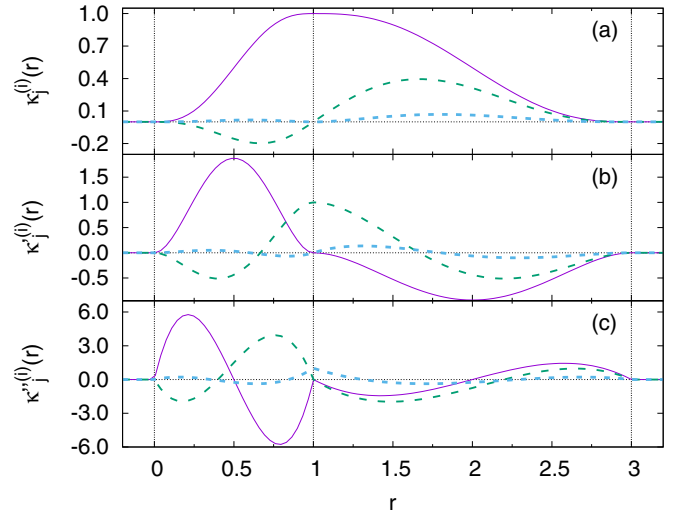

FIG. 1. (a) FEM functions (purple solid line) $\kappa_0^{(i)}(r)$, (green dashed line) $\kappa_1^{(i)}(r)$, and (blue dotted line) $\kappa_2^{(i)}(r)$ for $r_{i-1} = 0, r_i = 1$, and $r_{i+1} = 3$. (b) First and (c) second derivatives of the FE functions.

polynomials satisfying the boundary conditions

$$\frac{d^k P_j}{dx^k}(0) = \delta_{j,k}, \qquad \frac{d^k P_j}{dx^k}(1) = 0, \qquad (12a)$$

$$\frac{d^k Q_j}{dx^k}(0) = 0, \qquad \frac{d^k Q_j}{dx^k}(1) = \delta_{j,k}. \qquad (12b)$$

where $j, k = 0, 1, 2$. These functions are defined to vanish everywhere outside $[0,1]$ and read

$$Q_0(x) = x^3[6x^2 - 15x + 10], \qquad (13a)$$

$$Q_1(x) = -x^3[3x^2 - 7x + 4], \qquad (13b)$$

$$Q_2(x) = \frac{x^3}{2}[x - 1]^2, \qquad (13c)$$

with $Q_j(x < 0) = Q_j(x > 1) = 0$ and $P_j(x) = (-1)^j Q_j(1 - x)$. The FE functions $\kappa_j^{(i)}(r)$, defined on the interval $r \in [r_{i-1}, r_{i+1}]$, are built by gluing together P_j and Q_j, which are scaled appropriately such that $\kappa_j^{(i)}(r)$ and its first derivative are smooth functions. The FE functions read

$$\kappa_j^{(i)}(r) = (r_i - r_{i-1})^j Q_j\left(\frac{r - r_{i-1}}{r_i - r_{i-1}}\right)$$

$$+ (r_{i+1} - r_i)^j P_j\left(\frac{r - r_i}{r_{i+1} - r_i}\right), \qquad (14)$$

with $\partial_r^k \kappa_j^{(i)}(r_{i'}) = \delta_{j,k}\delta_{i,i'}$. In Fig. 1, the three types of FE functions are shown for $r_{i+1} - r_i \neq r_i - r_{i-1}$. The FE functions at the boundaries are special because the points r_0 and r_{N+1} do not exist. This can be easily cured by just dropping the term Q_j or P_j for the r_1 or r_N boundaries, respectively. The functions $\kappa_0^{(1)}(r)$ and $\kappa_0^{(N)}(r)$ are ignored to ensure the boundary

conditions $u_{n,l}(0) = u_{n,l}(r_{max}) = 0$. The overall number of FE functions for N reference points r_i is $N_b = 3N - 2$.

The FE functions are not orthogonal to each other, which introduces nontrivial overlap matrices $\langle \kappa_j^{(i)} | \kappa_{j'}^{(i')} \rangle \neq \delta_{j,j'} \delta_{i,i'}$. As a consequence, the Hartree–Fock orbital equations turn into a generalized eigenvalue problem as in the case of Gaussian or B-spline representations. Due to its construction, an FE function overlaps only with the FE functions centered around the same or neighboring grid points, $\langle \kappa_j^{(i)} | \hat{A} | \kappa_{j'}^{(i')} \rangle = 0$ if $|i - i'| > 1$.

3. Finite-element discrete-variable representation

The finite-element discrete-variable representation (DVR) is based on the FEM method described in Sec. II B 2. To avoid the issue of nonorthogonal basis sets and recovering a representation in which local operators are diagonal matrices, we introduce a basis transformation, $v_k(r) = \sum_{j,i} T_{j,i}^k \kappa_j^{(i)}(r)$, such that the position operator $\hat{r}$ becomes diagonal,

$$\hat{r} | v_k \rangle = r_k | v_k \rangle, \quad (15)$$

where the eigenvalues r_k are distinctly different from the r_i, which are the reference grid points for the FE functions. To find the coefficients $T_{j,i}^k$, we need to solve the generalized eigenvalue problem

$$\sum_{i',j'} \langle \kappa_j^{(i)} | \hat{r} | \kappa_{j'}^{(i')} \rangle T_{j',i'}^k = r_k \sum_{i',j'} \langle \kappa_j^{(i)} | \kappa_{j'}^{(i')} \rangle T_{j',i'}^k. \quad (16)$$

Having $3N - 2$ FE functions leads to $3N - 2$ eigenvalues r_k. The new DVR basis functions $v_k(r)$ are orthogonal to each other, $\int dr \, v_k(r) v_{k'}(r) = \delta_{k,k'}$. Note that the DVR and FEM bases are equivalent because they describe exactly the same radial configuration space.

Even though $\{v_k(r)\}$ is a set of orthogonal functions that diagonalize $\hat{r}$ (in the FEM representation), they do not diagonalize all local functions, $\langle v_k | V(\hat{r}) | v_{k'} \rangle \neq V(r_k) \delta_{k,k'}$, because the underlying FEM basis is not a complete basis. Strictly speaking, any operator A^{FEM} in the FEM representation has to be rewritten in the DVR basis via the basis transformation

$$A^{DVR} = T A^{FEM} T^{-1}, \quad (17)$$

where T is the transformation matrix with the entries $T_{j,i}^k$ defined in Eq. (16).

However, to recover the diagonal representation of local operators, we use the standard DVR approximation, $\langle v_k | V(\hat{r}) | v_{k'} \rangle \approx V(r_k) \delta_{k,k'}$. After this approximation, the DVR representation is no longer equivalent to the FEM representation. In Sec. III, we discuss the practical implication of this approximation.

C. Absorbing boundaries

To avoid very large numerical boxes, we introduce boundary conditions shortly before the numerical box ends. There are several ways to do this. A conceptually simple method is to use a complex absorbing potential (CAP), where a purely imaginary local potential is introduced. A very commonly used CAP is [36,59]

$$W(r) = -i\eta \, (r - r_{absorb})^2 \, \Theta(r - r_{absorb}), \quad (18)$$

where η is real and defines the absorption strength. The CAP is a one-particle operator and acts on each particle independently. In CIS, only one electron is allowed to be ionized, so only one electron will be affected by the CAP. We have used this CAP successfully in the past (see, e.g., Refs. [25,32,44,51]). However, CAPs are not perfect absorbers and always lead to artificial reflections, which can lead to difficulties for time-dependent problems especially when calculating photoelectron spectra [44].

Another method to create absorbing boundaries is exterior complex scaling (ECS) [36,37]. ECS is based on an analytic continuation of the radial coordinate into the complex plane starting at a radius r_{absorb} which is not the origin. Beyond r_{absorb}, the complex path is usually rotated by a specific angle θ into the complex plane. In the limit of an exact representation (infinite basis set), ECS yields exact Siegert energies for quasi-bound states [36] and can be used as a perfect absorber [39,60] without reflections.

There exist two types of ECS [37]: hard and smooth ECS. For hard ECS the complex scaling starts abruptly at r_{absorb} whereas for smooth ECS (SES) the complex scaling starts—as the name says—smoothly around r_{absorb}. The form of SES that we consider reads [61]

$$r \rightarrow \rho(r) = r + (e^{i\theta} - 1) \left[r + \lambda \ln \left(\frac{1 + e^{(r_{absorb} - r)/\lambda}}{1 + e^{r_{absorb}/\lambda}} \right) \right], \quad (19)$$

where λ defines the smoothness of the onset of complex scaling. Asymptotically we find $\rho(r \ll r_{absorb}) \approx r$ and $\rho(r \gg r_{absorb}) \approx r_{absorb} + e^{i\theta}(r - r_{absorb})$ assuming that r_{absorb} is far from the origin ($r_{absorb} \gg \lambda$). This is exactly what we want. Close to the origin we have an unscaled (the original) radial coordinate and beyond r_{absorb} we have a coordinate r that is rotated into the complex plane. The angular coordinates (φ, ϑ) are not affected by this scaling.

The Hamiltonian for complex scaling, $\hat{H}^{SES}(t)$, is obtained by replacing r with $\rho(r)$. To ensure that only the radial degree of freedom is affected, the Hamiltonian and all other operators are first written in a form acting only on the radial orbital wave function $u_{n,l}(r)$ [see Eq. (6)]. This ensures that the volume element r^2 arising from the angular degrees of freedom and derivatives that couple radial and angular coordinates (e.g., ∂_z) are properly taken care of before complex scaling is performed.

The scaled Fock operator $\hat{H}_0^{SES}$ defining the scaled radial components $u_{n,l}(\rho)$ of the one-particle orbitals φ_p reads

$$\hat{H}_0^{SES} u_{n,l}(\rho) = \left[-\frac{1}{2} \partial_\rho^2 + \frac{l_n(l_n + 1)}{2\rho^2} - \frac{Z}{\rho} \right] u_{n,l}(\rho) + \sum_i [2 J_i(\rho) u_{n,l}(\rho) - K_i[u_{n,l}](\rho)], \quad (20)$$

where $\sum_i$ is the sum over all occupied orbitals and $2 J_i$ and K_i are the direct and exchange parts of the Hartree–Fock mean-field potential,

$$J_i(\rho) = (2l_i + 1) v^{(0)}(n_i, l_i; n_i, l_i, \rho), \quad (21a)$$

$$K_i[u_{n,l}](\rho) = \sum_L \left[C_{l,0;L,0}^{l_i,0} \right]^2 v^{(L)}(n_i, l_i; n, l, \rho) \, u_{n_i,l_i}(\rho), \quad (21b)$$

where $C_{l_1,m_1;l_2,m_2}^{l_3,m_3}$ are a Clebsch–Gordan coefficients. The Coulomb integrals along the complex path C defined in Eq. (19) read

$$v^{(L)}(n_1,l_2;n_2,l_2,\rho_1) = \int_C d\rho \; \frac{\rho_>^L}{\rho_<^{L+1}} u_{n_1,l_1}(\rho) u_{n_2,l_2}(\rho)$$

$$= \int_0^\infty dr_2 \; \frac{\rho_>^L}{\rho_<^{L+1}} \tilde{u}_{n_1,l_1}(r_2) \tilde{u}_{n_2,l_2}(r_2), \quad (22)$$

where $\rho_> = \rho(r_>)$, $\rho_< = \rho(r_<)$, $\rho_1 = \rho(r_1)$ with $r_> = \max(r_1,r_2)$ and $r_< = \min(r_1,r_2)$. The volume element arising from the change in the integration parameter [$d\rho = \rho'(r)dr$] is absorbed in the definition of the orbitals, $\tilde{u}_{n,l}(r) = \sqrt{\rho'(r)}u_{n,l}(\rho(r))$. In a similar way, the scaled two-dimensional (2D) radial integrals of the electron-electron interaction appearing in $\hat{H}_1$ can be written.

For a scaled local one-particle potential $V(\rho)$, the radial integral of the matrix elements reads

$$(i|V(\rho)|j) = \int_C d\rho \; b_i(\rho) V(\rho) b_j(\rho)$$

$$= \int_0^\infty dr \; \tilde{b}_i(r) V(\rho(r)) \tilde{b}_j(r), \quad (23)$$

where $\tilde{b}_i(r) = \sqrt{\rho'(r)}b_i(\rho(r))$. Matrix elements for the first and second derivatives (as they appear in the momentum and kinetic-energy operators, respectively) read

$$(i|\partial_\rho|j) = \int_C d\rho \; b_i(\rho) \partial_\rho b_j(\rho)$$

$$= \int_0^\infty dr \; \tilde{b}_i(r) \left(\frac{1}{\rho'} \partial_r - \frac{\rho''}{2\rho'^2} \right) \tilde{b}_j(r), \quad (24a)$$

$$(i|\partial_\rho^2|j) = \int_C d\rho \; b_i(\rho) \partial_\rho^2 b_j(\rho)$$

$$= \int_0^\infty dr \; \tilde{b}_i(r) \left(\frac{1}{\rho'} \partial_r^2 \frac{1}{\rho'} + \frac{2\rho'''\rho' - 3\rho''^2}{4\rho'^4} \right) \tilde{b}_j(r)$$

$$= \int_0^\infty dr \; \tilde{b}_i(r) \left(-\overleftarrow{\partial}_r \frac{1}{\rho'^2} \overrightarrow{\partial}_r - \frac{2\rho'''\rho' - 5\rho''^2}{4\rho'^4} \right) \tilde{b}_j(r), \quad (24b)$$

where $\overleftarrow{\partial}_r$ ($\overrightarrow{\partial}_r$) means the derivative acts to the left (right). Derivatives without the directional arrow act (as always) to the right. There exist two equivalently symmetric expressions for the kinetic-energy operator for $\tilde{u}_{n,l}(r)$. In both cases new potentials appear. The symmetric expression $\frac{1}{\rho'} \partial_r^2 \frac{1}{\rho'}$ is used for PSG and DVR representations, where $\rho'(r)$ can be evaluated at the grid points. The second symmetric expression $\overleftarrow{\partial}_r \frac{1}{\rho'^2} \overrightarrow{\partial}_r$ is used for the FEM representation, where the radial derivatives act directly on the FEM basis functions.

Expectation values are calculated by using the unscaled operators with the integration along the real axis (not the complex path C) such that the integral yields a real number. Because the Hamiltonian is not Hermitian, it follows that $\langle\Psi(t)| \neq |\Psi(t)\rangle^\dagger$. Therefore, it is generally necessary to perform a separate time propagation for $\langle\Psi(t)|$. This is numerically challenging because the norm of $\langle\Psi(t)|$ goes to infinity as the norm of $|\Psi(t)\rangle$ goes to zero [62]. As an approximation, we just use

$\langle\Psi(t)| = |\Psi(t)\rangle^\dagger$, which means that the effect of the absorber gets imprinted on the expectation values whereas in the former case it would not. For the expectation values involving local [i.e., $V(r)$] and first-derivative (i.e., ∂_r) operators, the radial matrix elements read

$$\langle i|V|j\rangle = \int_0^\infty dr \; b_i^*(r) V(r) b_j(r)$$

$$= \int_0^\infty dr \; \tilde{b}_i^*(r) \frac{V(r)}{|\rho'(r)|} \tilde{b}_j(r), \quad (25a)$$

$$\langle i|\partial_r|j\rangle = \int_0^\infty dr \; b_i^*(r) \partial_r b_j(r)$$

$$= \int_0^\infty dr \; \tilde{b}_i^*(r) \left(\frac{1}{|\rho'(r)|} \partial_r - \frac{\rho''(r)}{2\rho'(r)|\rho'(r)|} \right) \tilde{b}_j(r). \quad (25b)$$

The same idea has been used by Moiseyev and Lein [63] to calculate time-dependent expectation values with complex scaling.

The orbital energies ε_p become complex due to the complex scaling. For large orbital energies, where the kinetic-energy contribution dominates, one finds $\varepsilon_a \to e^{-2i\theta}\varepsilon_a$ [36]. Resonances that are imbedded in the continuum will generally stand out when $\theta_{\rm res} < 2\theta$, where $\theta_{\rm res} = -\arg[E_{\rm res}]$ is the angle of the complex-valued resonance energy $E_{\rm res}$, and θ is the complex scaling angle [cf. Eq. (19)]. The imaginary part of the resonance energy, $\text{Im}\{E\} = -\Gamma/2 = -1/(2T)$, is directly related to the inverse lifetime.

By taking the difference between the scaled and unscaled Hamiltonians, we can define a complex absorbing potential, $\hat{W}^{\rm SES} = \hat{H}_0^{\rm SES} - \hat{H}_0$, where $\hat{H}_0$ is the unscaled Fock operator [64]. The complex absorbing potential for SES is not local due to the scaled kinetic operator. Complex scaling absorbs an escaping electron equally well regardless of its energy in contrast to a CAP absorber. For ECS in a finite grid representation, this statement is not strictly true anymore [47]. Nevertheless, the absorption is less energy dependent than for a local CAP.

III. RESULTS

A. High-harmonic generation

In this section, we compare the three grid representations (PSG, FEM, and DVR) and the two absorption methods (CAP and SES) with each other for an HHG scenario in atomic hydrogen. We treat the light-matter interaction in the velocity and length gauges. The vector potential of the strong-field pulse is given by

$$\mathcal{E}(t) = -E_0 \mathbf{e}_z \left[\sin^2\left(\frac{\pi t}{T}\right) \cos(\omega_0 t) \right.$$

$$\left. + \frac{\pi}{\omega_0 T} \sin\left(\frac{2\pi t}{T}\right) \sin(\omega_0 t) \right], \quad (26a)$$

$$\mathcal{A}(t) = \frac{E_0 \mathbf{e}_z}{\omega_0} \sin^2\left(\frac{\pi t}{T}\right) \sin(\omega_0 t). \quad (26b)$$

TABLE I. Error ϵ for $\langle \dot{z} \rangle(t)$ is shown for different numbers of grid points, orbital energy cutoffs, and maximum angular momenta. The convergence with respect to these parameters is shown for the velocity and length gauges, where all other parameters are kept fixed at their reference values. The reference signal $\langle \dot{z} \rangle_{\text{ref}}(t)$ is calculated where all parameters are kept at their reference values: $N_b = 1200$, $e_c = 50$, $l_{\max} = 20$, $dt = 0.005$.

Grid points			Time step			Energy cutoff			Angular momentum		
N_b	ϵ_{length}	$\epsilon_{\text{velocity}}$	dt	ϵ_{length}	$\epsilon_{\text{velocity}}$	e_c	ϵ_{length}	$\epsilon_{\text{velocity}}$	$l_{\max}$	ϵ_{length}	$\epsilon_{\text{velocity}}$
300	1.5×10^{-6}	2.6×10^{-6}	0.01	4.6×10^{-11}	2.8×10^{-9}	2	1.2×10^{-4}	8.1×10^{-2}	4	3.7×10^{-3}	2.8×10^{-3}
600	1.5×10^{-6}	1.7×10^{-6}	0.025	1.6×10^{-10}	1.3×10^{-7}	10	3.3×10^{-7}	3.3×10^{-3}	8	1.9×10^{-4}	8.02×10^{-6}
900	1.4×10^{-6}	1.4×10^{-6}	0.05	3.9×10^{-9}	2.6×10^{-6}	20	1.8×10^{-8}	6.2×10^{-4}	12	1.4×10^{-5}	1.5×10^{-8}

It coincides with the pulse [65] used in Ref. [66]. The carrier frequency, $\omega_0 = 0.057$ a.u., corresponds to a wavelength of 800 nm and an optical cycle of $\tau = 110.32$ a.u. The pulse duration is $T = 3\tau$ and the electric field of $E_0 = 0.029$ a.u. corresponds to the cycle-averaged laser intensity of 3×10^{13} W/cm^2.

1. Numerical convergence

First, we discuss the gauge-dependent convergence behavior with respect to the following physical and numerical variables: maximum orbital angular momentum $l_{\max}$, orbital energy cutoff e_c, the number of radial basis functions N_b, and the propagation time step dt. After we have identified a set of suitable parameters, we discuss the performances of the different absorber and grid representations. To study the convergence behavior, we compare the time-dependent momentum $\langle \dot{z} \rangle(t)$ of the electron and quantify the error by

$$\epsilon = \sqrt{\int_0^{t_{\max}} \left[\langle \dot{z} \rangle(t) - \langle \dot{z} \rangle_{\text{ref}}(t) \right]^2 dt}. \quad (27)$$

The subscription "ref." stands for the converged reference signal. Note that, for the velocity gauge, the instantaneous velocity of the electron is given by $\langle \dot{z} \rangle(t) = \langle p - \mathcal{A} \rangle(t)$, which is shifted by the vector potential $-\mathcal{A}(t)$ and does not coincide with the canonical momentum $\langle p \rangle(t)$. The electron motion is calculated up to the end of the pulse at $t_{\max} = 331$ using a fourth-order Runge–Kutta propagator.

The box size is set to $r_{\max} = 125$ with a CAP of strength $\eta = 0.002$ starting at $r_{\text{absorb}} = 100$. The CAP parameters are chosen to be quite similar to previous calculations [20,32,51]. The box size and the beginning of the CAP radius are well beyond the classical turning point radius, which is $E_0/\omega^2 = 8.9$, such that the CAP has no influence on the dynamics. The nonlinear radial mapping of Eq. (8) with $\zeta = 1$ is used for all three radial representations. In this section, we limit ourselves to the PSG representation because all three grid methods show identical convergence behavior for the variables discussed here.

In Table I, the convergence of the error, ϵ, for the variables mentioned above is shown for both the velocity and length gauges. Only one parameter is changed at a time, keeping all other parameters fixed at their reference values ($N_b = 1200$, $e_c = 50$, $l_{\max} = 20$, $dt = 0.005$). The result where all parameters have their reference value constitutes the reference signal, $\langle \dot{z} \rangle_{\text{ref}}(t)$. To get an idea to what the values in Table I correspond, the time-dependent signal $\langle \dot{z} \rangle(t)$ is shown for several listed parameters in Fig. 2. Calculations with errors

below 10^{-4} can be considered converged. Thanks to the nonlinear grid, already for 300 basis functions (three basis functions per atomic unit) the results are converged for both gauges. A time step of $dt = 0.05$ is sufficient to obtain converged results. In the length gauge, the convergence with respect to dt occurs faster than in the velocity gauge which is in part due to the larger spectral range of orbitals φ_p needed to get converged results.

The orbital energy cutoff e_c and the angular momentum $l_{\max}$ convergences are gauge dependent. The number of angular momenta required to obtain converged results is smaller for the velocity gauge than for the length gauge. We find that $l_{\max} = 8$ is enough for the velocity gauge whereas the length gauge requires $l_{\max} = 12$ for the same level of convergence. This is a 50% increase in the angular momentum needed for the length gauge. This trend agrees with the finding in Ref. [66].

The orbital energy cutoff convergence is much faster for the length gauge, which is already converged for $e_c = 2$, than for the velocity gauge, which requires $e_c \geqslant 20$ to reach a converged level. Since we solve the equation of motion [see Eq. (5)] in an orbital representation and not in a grid representation, the orbital energy cutoff has a similar effect as the number of grid points used in Ref. [66]. More specifically, the orbital energy cutoff is an additional layer (besides the number of radial basis functions) of controlling the radial representation that does not exist in a grid representation. The orbital energy cutoff restriction is based on the idea that very
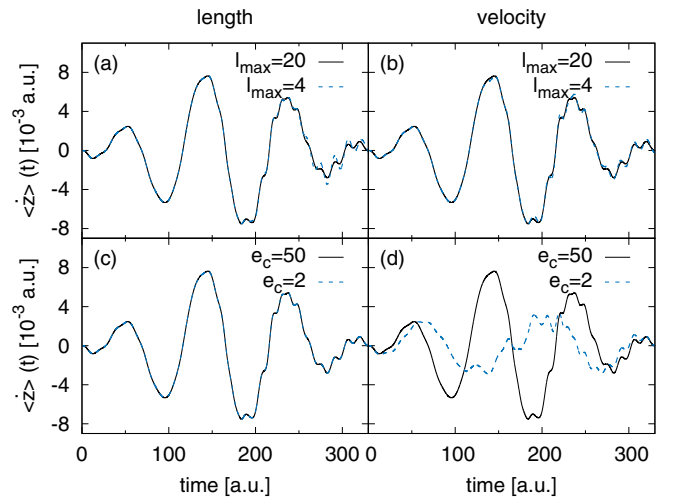

FIG. 2. The expectation value $\langle \dot{z} \rangle(t)$ for different $l_{\max}$ and e_c calculated (a), (c) in the length and (b), (d) in the velocity gauges. All other parameters are kept fixed at their reference values (see Table I).
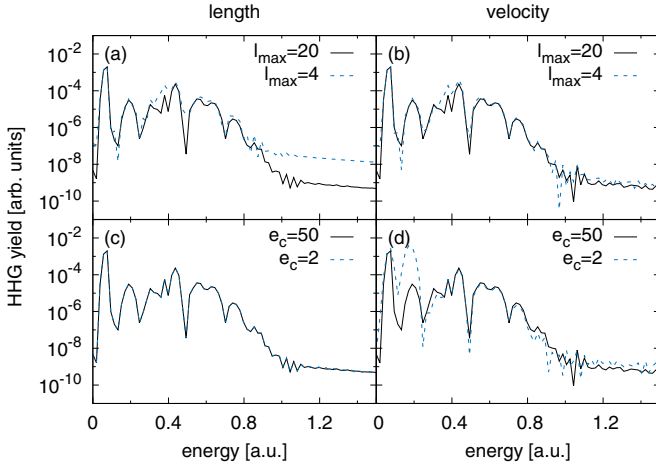
FIG. 3. HHG spectra corresponding to the results shown in Fig. 2. The HHG spectra are calculated with $\langle \dot{z} \rangle (t)$.
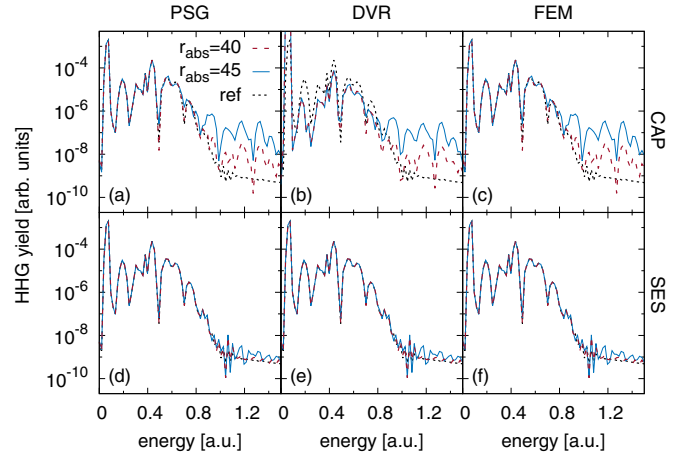

FIG. 4. HHG spectra in the velocity gauge for (a), (d) PSG, (b), (e) DVR, and (c), (f) FEM radial basis sets. Results in the upper panels (a)–(c) are based on a CAP absorber, and an SES absorber is used in the lower panels (d)–(f). The radius of the numerical box is 50 and the absorber starts around 40 (red dashed line) and 45 (blue solid line). The black dotted lines indicate the converged reference HHG spectrum.

high energy orbitals, which correspond to high kinetic energies that do not appear in the laser-driven motion, can be ignored.

In the velocity gauge, the coupling to high-energy orbitals is enhanced in comparison to the length gauge, $\langle a|p|b \rangle = (E_a - E_b)\langle a|z|b \rangle$, which explains why the orbital energy cutoff e_c tends to be higher for the velocity gauge. Cutoff energies of $e_c = 2$ and $e_c = 20$ correspond to ~ 80 and ~ 250 radial orbitals, respectively. The number of radial orbitals enters quadratically in the numerical effort to solve Eq. (5), whereas l_{max} enters only linearly. This makes calculations in the velocity gauge generally more demanding, which is opposite to the finding in Ref. [66] because of the significant reduction in radial basis functions by introducing an orbital cutoff energy.

In Fig. 3, the corresponding HHG spectra for the time traces shown in Fig. 2 are displayed. The HHG spectrum $S(\omega) \propto |\int [\partial_t \langle \dot{z} \rangle (t)] e^{-i\omega t} dt|^2$ is calculated with the dipole velocity [67]. The gauge choice does not matter once convergence is reached, demonstrating the gauge independence of physical observables. Similarly to the time trace, the HHG spectrum converges faster with increasing angular momentum for the velocity gauge and faster with increasing e_c for the length gauge. The large angular momenta are needed to converge the middle and high-energy end of the HHG spectrum whereas the orbital energy cutoff affects mostly the low-energy part of the HHG spectrum.

In the following, we use $N_b = 3r_{max} + 1$ radial basis functions for all grids and gauges. For the length gauge we use $l_{max} = 15$ and $e_c = 5$, and for the velocity gauge we use $l_{max} = 10$ and $e_c = 20$.

2. Complex absorbing potential vs smooth exterior complex scaling

The absorbing region is an unwanted necessity to ensure that the electron gets properly absorbed. Keeping this region as small as possible without affecting performance is desirable. The ponderomotive quiver radius is $E_0/\omega^2 = 8.9$ for the pulse given in Eq. (26). A grid size of $r_{max} = 50$ should be quite sufficient to capture the laser-driven motion. In Figs. 4(a)–4(c) we compare the HHG for the CAP and in Figs. 4(d)–

4(f) we compare the SES absorbers starting at $r_{absorb} = 40$ and $r_{absorb} = 45$, corresponding to an absorption region with a width, $r_{max} - r_{absorb}$, of 10 and 5, respectively. The CAP strength is $\eta = 2 \times 10^{-3}$ and for SES the rotation angle is chosen to be $\theta = 25°$ and the smoothing parameter is $\lambda = 2$.

For the CAP absorber, both absorption regions are too small and large numerical noise appears around and beyond the cutoff region. From previous calculations we know that a CAP needs an absorption region with a width of 20–30 to perform well. The poor CAP performance for these small regions is, therefore, not a surprise because significant parts of the ionized electron wave packet do not get absorbed and instead get reflected. The SES, on the other side, performs well for absorbing regions as small as 5. This is in agreement with earlier findings for field-free wave-packet dynamics [47].

The small required absorbing region for SES allows us to reduce r_{max} even further. In Fig. 5, the system radius r_{max} is varied for SES by using an absorption region with a width of 10. The HHG spectrum starts to be affected by the system radius for $r_{max} \leqslant 20$ with the absorption starting
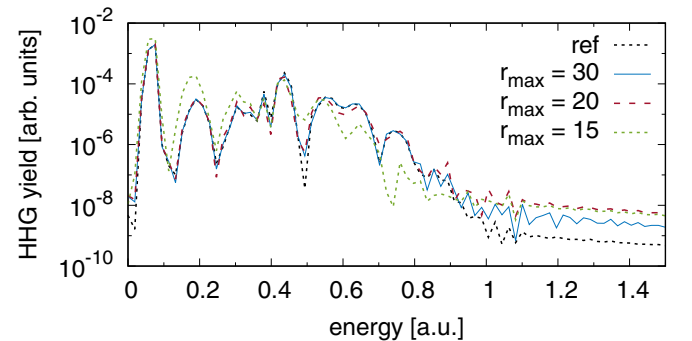

FIG. 5. HHG spectra for different r_{max} keeping the width of the absorbing region fixed at 10. The black dotted line indicates the converged reference HHG spectrum. All calculations are done in the FEM representation by using the SES absorber.
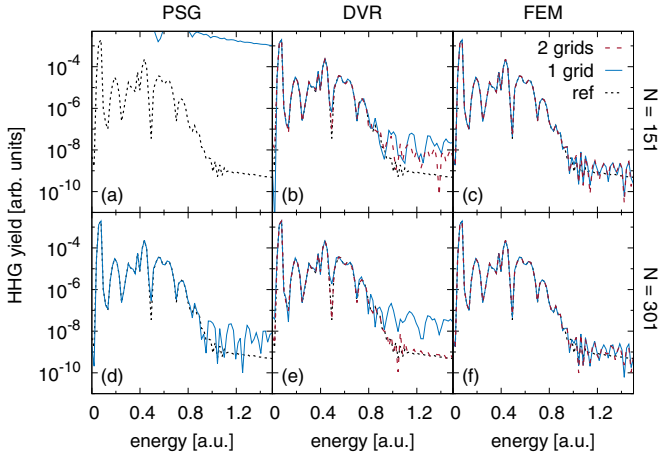
FIG. 6. HHG spectra for (a), (d) PSG, (b), (e) DVR, and (c), (f) FEM representation are shown for different grid-point distributions. A single Möbius-type grid (solid blue lines) and two Möbius-type grids (dashed red lines) concatenated at $r = 35a_0$ are used. For the PSG grid method, only the single Möbius-type grid is used. Results are shown for (a)–(c) 151 and (d)–(f) 301 radial basis functions. The black dotted lines indicate the reference HHG spectrum. In all cases SES is used with $\lambda = 0.1$.

around $r_{\text{absorb}} \leqslant 10$. This is not surprising because the absorber overlaps with the region of the electron trajectories that can return to the core and, hence, affects their motion.

3. Pseudospectral grid method vs finite-element method vs finite-element discrete-variable representation

An advantage of the FEM and DVR methods is that the grid points can be chosen arbitrarily without introducing a new coordinate transformation. Particularly for SES and the smooth turn-on of the complex scaling, which introduces a new complex potential, a denser grid may be required. In Fig. 6, HHG spectra for all three grid methods are shown for one Möbius-like grid distribution [see Eq. (8)] and two Möbius-like grid distributions concatenated at radius $r = 35$. The total number of radial basis functions is 151 [Figs. 6(a)–6(c)] and 301 [Figs. 6(d)–6(f)]. For the PSG grid, we only use the one-grid distribution because non-Möbius-like coordinate transformations $r \rightarrow r(x)$ introduce new potentials when expressing the Hamiltonian in terms of $x \in [-1, 1]$, which is a necessity for the PSG method. The smoothing parameter of the SES is chosen to be quite sharp with $\lambda = 0.1$ helping to demonstrates the influence of the pseudolocal approximations of the PSG and DVR methods.

Using two concatenated grids, which leads to an increased grid density around $r \sim 35 - 40$, improves the results because the complex potential introduced by the coordinate transformation is better represented. This improvement becomes most visible for the DVR method with 301 radial basis functions [see Fig. 6(e)], where the concatenated grid leads to fully converged results. For the FEM method, the concatenated grid adds no significant improvement for both numbers of radial basis function, and already convergence is reached for $N_b = 151$ with the usual Möbius-like grid. This shows that the FEM representation leads to a better radial representation
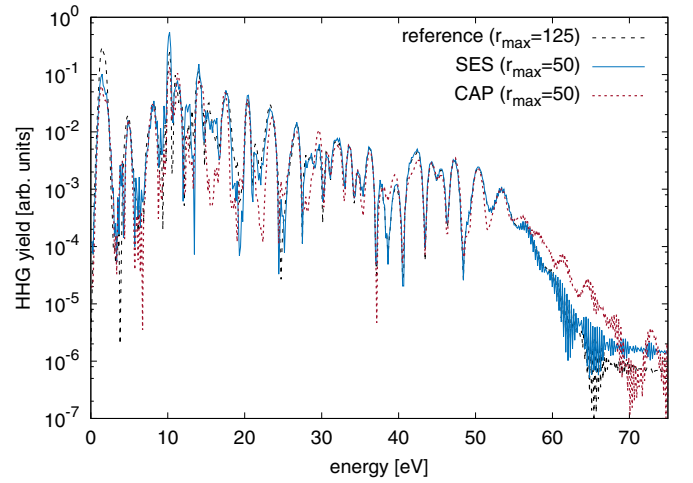
for the same number of radial functions than the DVR method, where local functions are approximated to be linear around the DVR points (see Sec. II B 3).

The PSG method shows much more inconsistent behavior. For $N_b = 151$ the calculations even diverge. A higher number of grid points ($N_b = 301$) generally helps but this is not always true. Increasing the number of radial functions to $N_b = 451$ (not shown) leads again to divergent results. This is also the case for smoother SES scaling of $\lambda = 1.0$ (not shown). In the DVR and FEM grid representations, the results always improve as the number of grid points increases.

4. High intensity

To show the applicability at high intensities, we study the HHG spectrum generated by a 5 fs FWHM Gaussian pulse with a (cycle-averaged) peak intensity of 2×10^{14} W/cm^2 and a wavelength of 800 nm. The HHG spectra shown in Fig. 7 are calculated for SES and CAP absorbers in the FEM representation and a box size of $r_{\text{max}} = 50$. The absorbing regions are 10 and 20 a.u. wide for the SES and CAP absorbers, respectively. The CAP strength is $\eta = 0.002$. For the SES absorber, we used $\theta = 25°$ and $\lambda = 2$. The spectra are converged with $l_{\text{max}} = 30$. The reference spectrum [68] is calculated with a larger box size, $r_{\text{max}} = 125$, such that the absorber has a negligible effect on the field-driven motion.

The SES results agree almost perfectly with the reference spectrum. The only notable difference is the very first peak at the driving frequency ω, which is technically not part of the HHG spectrum and is not of great interest. This discrepancy is understandable as very low electrons perform large excursions. Already the average extent of the ponderomotive quiver motion is 23 and covers almost half the box size of $r_{\text{max}} = 50$. All higher energies are well reproduced by using the SES absorber. The CAP, due to its larger extent, starts just a few atomic units after the classical turning point and affects the HHG spectrum at all photon energies up to the cutoff region.

FIG. 7. HHG spectra for the SES (solid blue line) and CAP (dotted red line) absorbers for a 2×10^{14} W/cm^2 pulse. The box radius is 50. The reference spectrum (dashed black line) is calculated with a box size of 125.
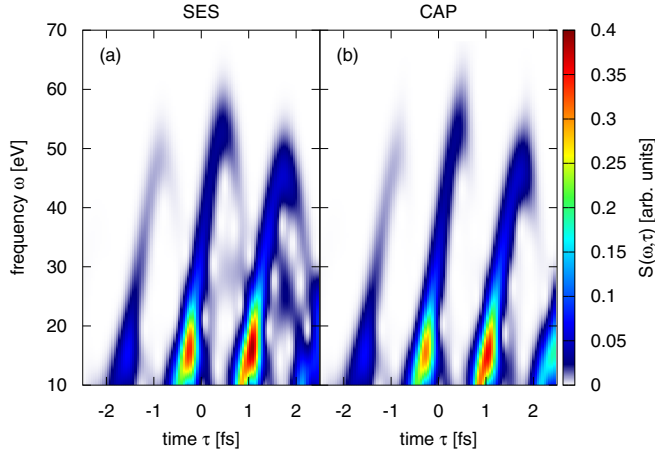
FIG. 8. The Gabor transformation associated with the HHG spectra in Fig. 7 calculated with (a) SES and (b) CAP absorbers. The Gabor window function has a Gaussian profile with a width of 6 a.u. (194 as).

The influence of the early turn-on of the CAP absorber can be clearly seen in the Gabor analysis (see Fig. 8). When using a CAP [see Fig. 8(b)], the "right" arms of the energy outbursts, which correspond to the long trajectories, are notably suppressed for all three instances in comparison to the SES absorber [see Fig. 8(a)].

B. Photoionization

Extreme ultraviolet photoionization

In this section, we compare the three grid methods for photoionization of argon with a 105 eV pulse with a duration of 1.21 fs (50 a.u.) and a peak intensity of 87.5 TW/cm^2 ($E = 0.05$ a.u.). In an earlier study [44], we investigated the convergence behavior of the t-SURFF method for calculating the photoelectron spectra (PES) of argon. In that study, the CAP has been used as an absorber and a strong dependence on the CAP strength η and the distance of the t-SURFF radius r_{tsurff} to r_{absorb} has been found. An absorber–t-SURFF distance of at least $r_{\mathrm{absorb}} - r_{\mathrm{tsurff}} = 20$ was found to be optimal. It is desirable to reduce this distance and make it less sensitive to the parameters of the absorber.

In Fig. 9, we compare the PES calculated in the velocity gauge by using CAP and SES absorbers both starting at $r_{\mathrm{absorb}} = 120$ and the t-SURFF radius is at $r_{\mathrm{tsurff}} = 100$. The PES shows two peaks at 76 and 89 eV corresponding to the ionization of a 3s and 3p electron, respectively.

For all the grids, the CAP strength η and the SES smoothing parameter λ are varied, respectively. The SES rotation angle is fixed at $\theta = 25°$. Identical results are obtained with $\theta = 10°$ (not shown) demonstrating the very weak dependence of the PES on the details of the SES absorber. The number of radial basis functions is $N_b = 901$ with a system radius of $r_{\mathrm{max}} = 150$, a Möbius-type grid distribution with $\zeta = 0.5$, and an orbital energy cutoff of $e_c = 20$.

The PSG grid results show for both absorber methods strong dependencies on the parameter of the absorber. For the ECS absorber at $\lambda = 1.0$ (cf. Fig. 9) the time propagation leads even to diverging results. In the case of a CAP absorber, the strong η
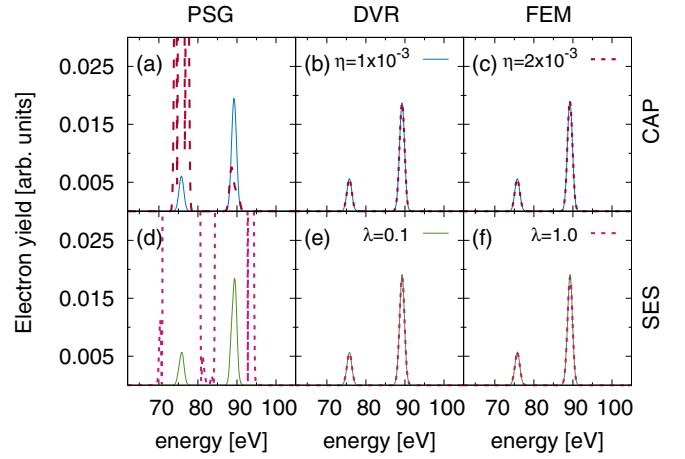

FIG. 9. Photoelectron spectrum (PES) of argon ionized by a 105 eV pulse with a duration of 1.21 fs (50 a.u.) and a peak intensity of 87.5 TW/cm^2. The PES are shown for all three grid methods (PSG, DVR, FEM) and both absorbers (CAP, SES), where the CAP strength η and the SES smoothing parameter λ are varied, respectively. The t-SURFF radius is $r_{\mathrm{tsurff}} = 100$ and the absorber starts at $r_{\mathrm{absorb}} = 120$.

dependence agrees with the finding in Ref. [44]. Surprisingly, this dependence is basically gone for FEM and DVR grid methods.

As the CAP introduces no discontinuities in the potential, which could lead to reflection, the volatile behavior of PSG must be attributed to the way the flux at the radius, r_{tsurff}, is calculated. For the DVR and FEM methods, the derivative can be analytically found by calculating the derivative of the FEM functions. In case of the PSG method, the derivative is a highly nonlocal operator that scales like $(x_i - x_j)^{-1}$, where $x_{i/j}$ are the roots of a Legendre polynomial (see Sec. II B 1 and Ref. [54]). This makes the derivative much more dependent on the wave function near the absorber whereas for DVR and FEM the derivative at r_{tsurff} depends only on the parts of the wave function that are in the vicinity of r_{tsurff} [69].

In the strong-field regime, we have seen in Sec. III A that a shorter absorbing region is possible when using SES. The same should be true for absorbing the photoelectron ionized by one-photon absorption. In Fig. 10, we compare the PES of the ionized 3p electron for different values of r_{tsurff} and r_{absorb} for all three grids by using the SES method. Again, the PSG grid method shows strong fluctuations in the spectrum as the absorbing region varies. For $r_{\mathrm{tsurff}} = 100$, $r_{\mathrm{absorb}} = 120$ (solid blue line), the PES peak is slightly deformed and not fully symmetric. Reducing the width of the absorbing region to 10 [see red dashed line in Fig. 10(a)] improves the spectrum. However, smaller absorbing regions below 10 are not beneficial and very quickly lead to highly distorted spectra.

For the DVR method, the dependence on the SES parameters is significantly reduced. Only when $r_{\mathrm{tsurff}} = r_{\mathrm{absorb}}$ does the photoelectron peak start to show small deformations. With the FEM grid method, it is even possible to calculate the PES when choosing $r_{\mathrm{tsurff}} = r_{\mathrm{absorb}}$ and having an absorbing region as small as $r_{\mathrm{max}} - r_{\mathrm{absorb}} = 5$. This is a large reduction of the required radial space by an order of magnitude as compared to using a CAP absorber.
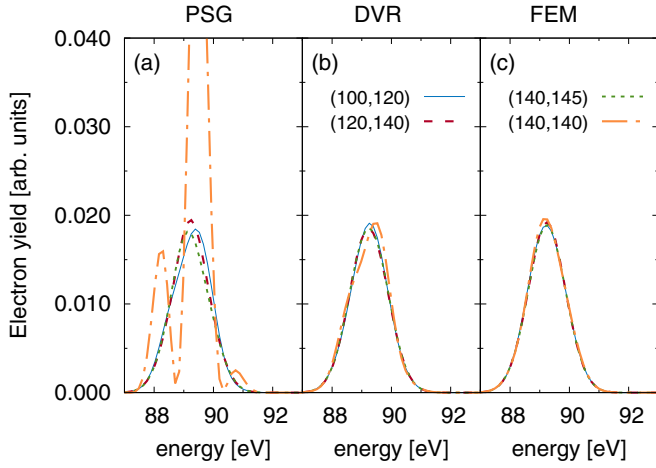
FIG. 10. Photoelectron spectrum (PES) of the ionized $3p$ electron of argon for all three grids using the SES absorber. The t-SURFF radius r_{tsurff} and the SES absorber radius r_{absorb} are varied, indicated by (r_{tsurff}, r_{absorb}). The SES smoothing parameter is $\lambda = 0.1$ and the SES angle is $\theta = 25°$. The pulse is the same as in Fig. 9.

C. Strong-field ionization

After studying the photoelectron spectrum in the one-photon limit, we investigate briefly the performance in the multiphoton limit in hydrogen, where more than one photon is required to ionize the system. We choose the 20 cycle pulse of Ref. [70], which is given by $A(t) = \frac{E_0}{\omega_0} \cos^2(\pi t/T) \cos \omega_0 t$, with frequency $\omega_0 = 0.114$ (400 nm), intensity 10^{14} W/cm^2 ($E_0 = 0.535$), and duration $T = 20T_{\omega_0} = 40\pi/\omega_0$ [71]. The corresponding photoelectron spectra calculated with the FEM representation and a SES absorber are shown in Fig. 11 for a box size of (solid red line) $r_{\text{max}} = 70$ with $r_{\text{tsurff}} = 30$ and (dotted blue line) $r_{\text{max}} = 150$ with $r_{\text{tsurff}} = 125$. In both cases, the SES absorbing region starts at $r_{\text{absorb}} = r_{\text{max}} - 20$ with a smooth onset of $\lambda = 0.2$ and an angle of $\theta = 40°$. The
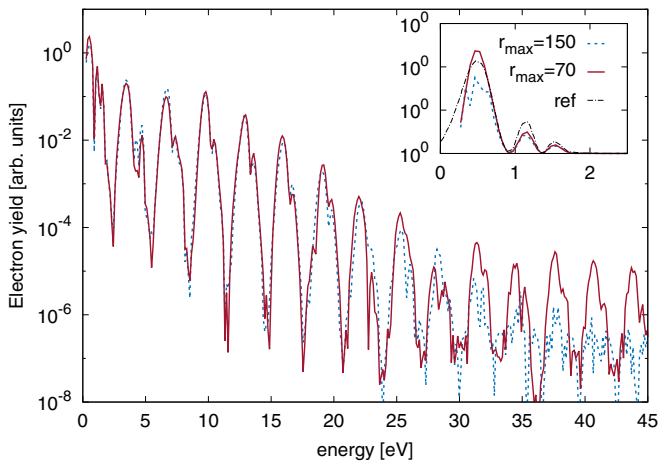

FIG. 11. ATI photoelectron spectrum of hydrogen ionized by a 20-cycle $\cos^2$ pulse with a wavelength of 400 nm and 10^{14} W/cm^2 peak intensity for a box size of (solid red line) $r_{\text{max}} = 70$ with $r_{\text{tsurff}} = 30$ and (dotted blue line) $r_{\text{max}} = 150$ with $r_{\text{tsurff}} = 125$. The FEM representation is used in combination with the SES absorber. The low-energy reference spectrum (dashed-dotted black line) is taken from Ref. [70].

results are not very sensitive to the exact shape of the SES absorber. The spectra are converged with respect to the orbital energy cutoff and the angular momentum which take the values $e_c = 20$ and $l_{\text{max}} = 30$, respectively.

The above-threshold ionization (ATI) peaks are clearly visible and located at their predicted positions, $n\omega_0 - I_p - U_p$, where $I_p = 0.5$ is the ionization potential of hydrogen, and $U_p = E_0^2/(4\omega_0^2) = 0.055$ (1.5 eV) is the ponderomotive potential, by which the continuum states are ac-Stark shifted in a laser field. The first photoelectron peak is shown in the inset with the reference spectrum of Ref. [70] (dashed-dotted black line). The substructure of the ATI peak is reproduced as well, which originates from the rising and falling edges of the pulse caused by a time-dependent ac-Stark shift of the continuum [70,72].

Even though the spectrum depends only slightly on SES parameters, it seems to be more sensitive to r_{tsurff}, indicating that the spectrum is not fully converged. Both curves demonstrate by how much the spectra usually change as r_{tsurff} is varied. The numerical noise level is around 10^{-7} which can be seen in the $r_{\text{max}} = 150$ spectrum at high energies. Also, the agreement with the reference spectrum at low energies is not perfect.

Here, we see the first limitations of using SES despite its good performance for HHG spectra at low and high pulse intensities. The use of a CAP absorber instead of SES leads to very similar results (not shown), demonstrating that the absorption of the photoelectron is not perfect for both absorbers. In comparison with the earlier discussions, the photoelectron spectrum in the strong-field regime is more sensitive to imperfections of the absorber than are photoelectron spectra in the UV regime or HHG spectra.

IV. CONCLUSION

We have studied the performance of smooth exterior complex scaling (SES) and a complex absorbing potential (CAP) for typical scenarios appearing in attosecond physics: computation of the HHG spectrum and the photoelectron spectrum in the one-photon and multiphoton regimes. For HHG spectra and photoelectron spectra in the one-photon limit, using SES to absorb the electron performs better and is more stable than a CAP absorber. Additionally, SES requires a much smaller radial region to absorb the photoelectron [47]. In the strong-field regime, both SES and CAP absorbers have to be carefully used because both absorbers seem to have difficulties to provide a fully converged photoelectron spectrum.

The nonlinear grid distribution leads to converged results with relatively few grid points. For the FEM and DVR (more precisely FEM-DVR) grid methods, an arbitrary distribution of grid points can be easily achieved without transforming the Hamiltonian—opposite to the PSG grid method. Generally, DVR and FEM prove to be more stable grid methods than PSG for strong-field as well as for attosecond XUV ionization calculations. DVR and FEM show a reduced dependence on the details of the absorber compared to PSG. The t-SURFF radius can even be chosen at the onset of the complex scaled region without significantly reducing the accuracy in the FEM representation.

Overall, FEM as well as DVR combined with an SES absorber increase generally the stability for HHG and attosecond calculations and at the same time reduce the required system size and improve the computational performance. Only for photoelectron spectra in the strong-field regime, both absorbers have to be used with caution.

ACKNOWLEDGMENTS

[1] F. Krausz and M. Ivanov, Attosecond physics, Rev. Mod. Phys. **81**, 163 (2009).

[2] R. Pazourek, S. Nagele, and J. Burgdörfer, Attosecond chronoscopy of photoemission, Rev. Mod. Phys. **87**, 765 (2015).

[3] Z. Chang, P. B. Corkum, and S. R. Leone, Attosecond optics and technology: Progress to date and future prospects, J. Opt. Soc. Am. B **33**, 1081 (2016).

[4] J. L. Krause, K. J. Schafer, and K. C. Kulander, High-Order Harmonic Generation from Atoms and Ions in the High Intensity Regime, Phys. Rev. Lett. **68**, 3535 (1992).

[5] E. Constant, D. Garzella, P. Breger, E. Mével, Ch. Dorrer, C. Le Blanc, F. Salin, and P. Agostini, Optimizing High Harmonic Generation in Absorbing Gases: Model and Experiment, Phys. Rev. Lett. **82**, 1668 (1999).

[6] P. B. Corkum, Plasma Perspective on Strong Field Multiphoton Ionization, Phys. Rev. Lett. **71**, 1994 (1993).

[7] K. J. Schafer, Baorui Yang, L. F. DiMauro, and K. C. Kulander, Above Threshold Ionization Beyond the High Harmonic Cutoff, Phys. Rev. Lett. **70**, 1599 (1993).

[8] T. Popmintchev, M.-C. Chen, D. Popmintchev, P. Arpin, S. Brown, S. Ališauskas, G. Andriukaitis, T. Balčiunas, O. D. Mücke, A. Pugzlys, A. Baltuiška, B. Shim, S. E. Schrauth, A. Gaeta, C. Hernández-García, L. Plaja, A. Becker, A. Jaron-Becker, M. M. Murnane, and H. C. Kapteyn, Bright coherent ultrahigh harmonics in the keV x-ray regime from mid-infrared femtosecond lasers, Science **336**, 1287 (2012).

[9] T. Brabec and F. Krausz, Intense few-cycle laser fields: Frontiers of nonlinear optics, Rev. Mod. Phys. **72**, 545 (2000).

[10] J. Itatani, J. Levesque, D. Zeidler, H. Niikura, H. Pepin, J. C. Kieffer, P. B. Corkum, and D. M. Villeneuve, Tomographic imaging of molecular orbitals, Nature (London) **432**, 867 (2004).

[11] A. D. Shiner, B. E. Schmidt, C. Trallero-Herrero, H. J. Wörner, S. Patchkovskii, P. B. Corkum, J.-C. Kieffer, F. Legare, and D. M. Villeneuve, Probing collective multi-electron dynamics in xenon with high-harmonic spectroscopy, Nat. Phys. **7**, 464 (2011).

[12] M. C. H. Wong, A.-T. Le, A. F. Alharbi, A. E. Boguslavskiy, R. R. Lucchese, J.-P. Brichta, C. D. Lin, and V. R. Bhardwaj, High Harmonic Spectroscopy of the Cooper Minimum in Molecules, Phys. Rev. Lett. **110**, 033006 (2013).

[13] O. Smirnova, Y. Mairesse, S. Patchkovskii, N. Dudovich, D. Villeneuve, P. Corkum, and M. Yu. Ivanov, High harmonic interferometry of multi-electron dynamics in molecules, Nature (London) **460**, 972 (2009).

[14] D. Shafir, H. Soifer, B. D. Bruner, M. Dagan, Y. Mairesse, S. Patchkovskii, M. Yu. Ivanov, O. Smirnova, and N. Dudovich, Resolving the time when an electron exits a tunneling barrier, Nature (London) **485**, 343 (2012).

[15] P. M. Kraus, B. Mignolet, D. Baykusheva, A. Rupenyan, L. Horný, E. F. Penka, G. Grassi, O. I. Tolstikhin, J. Schneider,

F. Jensen, L. B. Madsen, A. D. Bandrauk, F. Remacle, and H. J. Wörner, Measurement and laser control of attosecond charge migration in ionized iodoacetylene, Science **350**, 790 (2015).

[16] M. Lein, Attosecond Probing of Vibrational Dynamics with High-Harmonic Generation, Phys. Rev. Lett. **94**, 053004 (2005).

[17] S. Baker, J. S. Robinson, C. A. Haworth, H. Teng, R. A. Smith, C. C. Chirilá, M. Lein, J. W. G. Tisch, and J. P. Marangos, Probing proton dynamics in molecules on an attosecond time scale, Science **312**, 424 (2006).

[18] W. Li, X. Zhou, R. Lock, S. Patchkovskii, A. Stolow, H. C. Kapteyn, and M. M. Murnane, Time-resolved dynamics in n2o4 probed using high harmonic generation, Science **322**, 1207 (2008).

[19] A. D. Bandrauk, S. Chelkowski, S. Kawai, and H. Lu, Effect of Nuclear Motion on Molecular High-Order Harmonics and on Generation of Attosecond Pulses in Intense Laser Pulses, Phys. Rev. Lett. **101**, 153901 (2008).

[20] S. Pabst, L. Greenman, D. A. Mazziotti, and R. Santra, Impact of multichannel and multipole effects on the Cooper minimum in the high-order-harmonic spectrum of argon, Phys. Rev. A **85**, 023411 (2012).

[21] O. Hassouneh, A. C. Brown, and H. W. van der Hart, Multichannel interference in high-order-harmonic generation from Ne$^+$ driven by an ultrashort intense laser pulse, Phys. Rev. A **89**, 033409 (2014).

[22] A. C. Brown, S. Hutchinson, M. A. Lysaght, and H. W. van der Hart, Interference Between Competing Pathways in Atomic Harmonic Generation, Phys. Rev. Lett. **108**, 063006 (2012).

[23] S. Pabst and R. Santra, Strong-Field Many-Body Physics and the Giant Enhancement in the High-Harmonic Spectrum of Xenon, Phys. Rev. Lett. **111**, 233005 (2013).

[24] M. B. Gaarde, C. Buth, J. L. Tate, and K. J. Schafer, Transient absorption and reshaping of ultrafast XUV light by laser-dressed helium, Phys. Rev. A **83**, 013419 (2011).

[25] S. Pabst, A. Sytcheva, A. Moulet, A. Wirth, E. Goulielmakis, and R. Santra, Theory of attosecond transient-absorption spectroscopy of krypton for overlapping pump and probe pulses, Phys. Rev. A **86**, 063411 (2012).

[26] J. Itatani, F. Quéré, G. L. Yudin, M. Yu. Ivanov, F. Krausz, and P. B. Corkum, Attosecond Streak Camera, Phys. Rev. Lett. **88**, 173903 (2002).

[27] P. M. Paul, E. S. Toma, P. Breger, G. Mullot, F. Augé, Ph. Balcou, H. G. Muller, and P. Agostini, Observation of a train of attosecond pulses from high harmonic generation, Science **292**, 1689 (2001).

[28] C. Ott, A. Kaldun, P. Raith, K. Meyer, M. Laux, J. Evers, C. H. Keitel, C. H. Greene, and T. Pfeifer, Lorentz meets Fano in spectral line shapes: A universal phase and its laser control, Science **340**, 716 (2013).

[29] Álvaro Jiménez-Galán, Luca Argenti, and Fernando Martín, Modulation of Attosecond Beating in Resonant Two-Photon Ionization, Phys. Rev. Lett. **113**, 263001 (2014).

[30] A. C. Brown, D. J. Robinson, and H. W. van der Hart, Atomic harmonic generation in time-dependent r-matrix theory, Phys. Rev. A **86**, 053420 (2012).

[31] L. Torlina, M. Ivanov, Z. B. Walters, and O. Smirnova, Time-dependent analytical r-matrix approach for strong-field dynamics. II. Many-electron systems, Phys. Rev. A **86**, 043409 (2012).

[32] L. Greenman, P. J. Ho, S. Pabst, E. Kamarchik, D. A. Mazziotti, and R. Santra, Implementation of the time-dependent configuration-interaction singles method for atomic strong-field processes, Phys. Rev. A **82**, 023406 (2010).

[33] H. M. and L. B. Madsen, Time-dependent restricted-active-space self-consistent-field theory for laser-driven many-electron dynamics, Phys. Rev. A **87**, 062511 (2013).

[34] T. Sato and K. L. Ishikawa, Time-dependent complete-active-space self-consistent-field method for multielectron dynamics in intense laser fields, Phys. Rev. A **88**, 023402 (2013).

[35] J. Caillat, J. Zanghellini, M. Kitzler, O. Koch, W. Kreuzer, and A. Scrinzi, Correlated multielectron systems in strong laser fields: A multiconfiguration time-dependent Hartree-Fock approach, Phys. Rev. A **71**, 012712 (2005).

[36] U. V. Riss and H. D. Meyer, Calculation of resonance energies and widths using the complex absorbing potential method, J. Phys. B: At., Mol. Opt. Phys. **26**, 4503 (1993).

[37] N. Moiseyev, Quantum theory of resonances: Calculating energies, widths and cross sections by complex scaling, Phys. Rep. **302**, 212 (1998).

[38] J. G. Muga, J. P. Palao, B. Navarro, and I. L. Egusquiza, Complex absorbing potentials, Phys. Rep. **395**, 357 (2004).

[39] A. Scrinzi, Infinite-range exterior complex scaling as a perfect absorber in time-dependent problems, Phys. Rev. A **81**, 053845 (2010).

[40] N. Rohringer, A. Gordon, and R. Santra, Configuration-interaction-based time-dependent orbital approach for *ab initio* treatment of electronic dynamics in a strong optical laser field, Phys. Rev. A **74**, 043420 (2006).

[41] X. M. Tong and N. Toshima, Controlling atomic structures and photoabsorption processes by an infrared laser, Phys. Rev. A **81**, 063403 (2010).

[42] C. W. McCurdy, C. K. Stroud, and M. K. Wisinski, Solving the time-dependent Schrödinger equation using complex-coordinate contours, Phys. Rev. A **43**, 5980 (1991).

[43] D. A. Telnov and S.-I. Chu, Multiphoton detachment of H^- near the one-photon threshold: Exterior complex-scaling–generalized pseudospectral method for complex quasienergy resonances, Phys. Rev. A **59**, 2864 (1999).

[44] A. Karamatskou, S. Pabst, Y.-J. Chen, and R. Santra, Calculation of photoelectron spectra within the time-dependent configuration-interaction singles scheme, Phys. Rev. A **89**, 033415 (2014).

[45] J. Bengtsson, E. Lindroth, and S. Selstø, Solution of the time-dependent Schrödinger equation using uniform complex scaling, Phys. Rev. A **78**, 032502 (2008).

[46] F. He, C. Ruiz, and A. Becker, Absorbing boundaries in numerical solutions of the time-dependent Schrödinger equation on a grid using exterior complex scaling, Phys. Rev. A **75**, 053407 (2007).

[47] R. Zavin, I. Vorobeichik, and N. Moiseyev, Motion of wave packets using the smooth-exterior-scaling complex potential, Chem. Phys. Lett. **288**, 413 (1998).

[48] S. Pabst, L. Greenman, A. Karamatskou, Y.-J. Chen, A. Sytcheva, O. Geffert, and R. Santra, XCID program package for multichannel ionization dynamics, 2016, Revision (Git): e44fcb7.

[49] L. Tao and A. Scrinzi, Photo-electron momentum spectra from minimal volumes: The time-dependent surface flux method, New J. Phys. **14**, 013021 (2012).

[50] A. Szabo and N. S. Ostlund, *Modern Quantum Chemistry* (Dover Publication Inc., Mineola, 1996).

[51] S. Pabst and R. Santra, Spin-orbit effects in atomic high-harmonic generation, J. Phys. B: At., Mol. Opt. Phys. **47**, 124026 (2014).

[52] The charge of the electron is set to $+1$.

[53] D. Krebs, S. Pabst, and R. Santra, Introducing many-body physics using atomic spectroscopy, Am. J. Phys. **82**, 113 (2014).

[54] J. Wang, S.-I. Chu, and C. Laughlin, Multiphoton detachment of H^-. II. Intensity-dependent photodetachment rates and threshold behavior—complex-scaling generalized pseudospectral method, Phys. Rev. A **50**, 3208 (1994).

[55] S. Pabst and R. Santra, Alignment of asymmetric-top molecules using multiple-pulse trains, Phys. Rev. A **81**, 065401 (2010).

[56] J. P. Boyd, *Chebyshev and Fourier Spectral Methods*, 2nd ed. (Dover, New York, 2001).

[57] T. N. Rescigno, M. Baertschy, D. Byrum, and C. W. McCurdy, Making complex scaling work for long-range potentials, Phys. Rev. A **55**, 4253 (1997).

[58] R. Santra, K. V. Christ, and C. H. Greene, Properties of metastable alkaline-earth-metal atoms calculated using an accurate effective core potential, Phys. Rev. A **69**, 042510 (2004).

[59] R. Santra, Why complex absorbing potentials work: A discrete-variable-representation perspective, Phys. Rev. A **74**, 034701 (2006).

[60] S. Klaiman, I. Gilary, and N. Moiseyev, Resonances for Coulombic potentials by complex scaling and free-reflection complex-absorbing potentials, Phys. Rev. A **70**, 012709 (2004).

[61] C. Buth and R. Santra, Theory of x-ray absorption by laser-aligned symmetric-top molecules, Phys. Rev. A **77**, 013413 (2008).

[62] N. Moiseyev, *Non-Hermitian Quantum Mechanics* (Cambridge University Press, Cambridge, UK, 2011).

[63] N. Moiseyev and M. Lein, Non-Hermitian quantum mechanics for high-order harmonic generation spectra, J. Phys. Chem. A **107**, 7181 (2003).

[64] C. Buth and R. Santra, Theory of x-ray absorption by laser-dressed atoms, Phys. Rev. A **75**, 033412 (2007).

[65] Our study revealed that in Ref. [66] a $\sin(\omega_0 t)$ pulse for the vector potential has been used to produce Figs. 1 and 2 and not a $\cos(\omega_0 t)$ carrier field as stated in Eq. (17). It was confirmed in a private communication with the authors.

[66] Y.-C. Han and L. B. Madsen, Comparison between length and velocity gauges in quantum simulations of high-order harmonic generation, Phys. Rev. A **81**, 063430 (2010).

[67] The HHG spectra calculated with $\langle z \rangle(t)$ (not shown) shows the same trends as the spectra calculated with $\langle dot05Fz \rangle(t)$.

[68] Parameter: PSG representation with $r_{max} = 125$ and $N_b = 750$. A CAP absorber is used with $r_{absorb} = 100$ and $\eta = 0.002$.

[69] The derivative of the wave function at r_{tsurff} depends on the absorber region as time evolves, but not instantaneously as is the case for the PSG method.

[70] C. Marante, L. Argenti, and F. Martin, Hybrid Gaussian–B-spline basis for the electronic continuum: Photoionization of atomic hydrogen, Phys. Rev. A **90**, 012506 (2014).

[71] Note that the CEP is shifted by 90° with respect to the pulse defined in Eq. (26).

[72] V. C. Reed and K. Burnett, Role of resonances and quantum-mechanical interference in the generation of above-threshold-ionization spectra, Phys. Rev. A **43**, 6217 (1991).